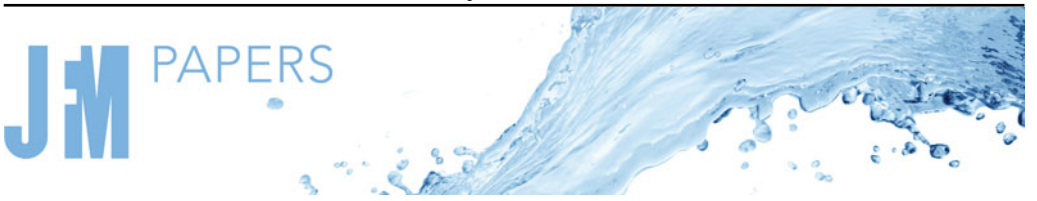
J. Fluid Mech. (2026), *vol.* 1035, A39, doi:10.1017/jfm.2026.11566



Structure of microlayer at water pool boiling for various bubble growth rates

Corentin Le Houedec[1], Boštjan Zajec[1], Cassiano Tecchio[1], Pere Roca i Cabarrocas[2], Pavel Bulkin[2] and Vadim S. Nikolayev[3]

[1]STMF, Université Paris-Saclay, CEA, Gif-sur-Yvette CEDEX 91191, France

[2]LPICM, CNRS, Ecole Polytechnique, Institut Polytechnique de Paris, Palaiseau 91120, France

[3]SPEC, CEA, CNRS, Université Paris-Saclay, Gif-sur-Yvette CEDEX 91191, France

Corresponding authors: Vadim S. Nikolayev, vadim.nikolayev@cea.fr; Cassiano Tecchio, cassiano.tecchio@cea.fr

(Received 20 November 2025; revised 3 March 2026; accepted 13 April 2026)

The growth of a single vapour bubble in a saturated pool of boiling water at atmospheric pressure on a transparent heater is investigated experimentally. The study focuses on a several microns thick liquid layer (called a microlayer) that can form between the heater and the bubble. The microlayer profile, the wall temperature distribution and the overall bubble shape are measured simultaneously and synchronously by white light interferometry, infrared thermography and sidewise shadowgraphy. To study the microlayer dynamics for different bubble growth rates, artificial cavities of different sizes were used. These control the wall superheating required for the bubble nucleation, i.e. the nucleation barrier. Both the bubble growth at its inertial stage and the microlayer parameters are found to be almost independent of the applied heat flux and controlled by the nucleation barrier only. The microlayer thickness and its area increase with the nucleation barrier. A model of microlayer formation based on an analogy with the Landau–Levich film deposition is further developed. By using it, the initial microlayer thickness, the time of microlayer formation at a given distance from the bubble centre and the radius of curvature of the bubble foot edge are recovered from the experimental data. The radius of curvature varies in time like the bubble radius, thus suggesting a self-similar bubble growth at its initial inertial stage. The coherency of the above model with the experimental results shows the model's validity.

Key words: boiling, contact lines, thin films

© The Author(s), 2026. Published by Cambridge University Press. This is an Open Access article, distributed under the terms of the Creative Commons Attribution licence (https://creativecommons.org/licenses/by/4.0/), which permits unrestricted re-use, distribution and reproduction, provided the original article is properly cited.

https://doi.org/10.1017/jfm.2026.11566 Published online by Cambridge University Press

1. Introduction

Boiling is widely used in many applications, from coffee making to energy conversion, phase separation in chemical engineering and cooling of power electronics. The bubble dynamics at boiling has been actively studied since the 1950s by analysing sidewise shadowgraphy images. It was found that there are two distinct bubble growth regimes. Right after the nucleation, the bubble growth is controlled by its growing pressure (Tong & Tang 2018) and the bubble radius is nearly linear in time. The growth is so fast that the inertia of the expelled liquid induces a downward-directed force that leads to the bubble 'flattening', hence, its hemispherical shape. This stage of growth is called inertial. At certain conditions (Snoeijer *et al.* 2006; Bureš & Sato 2021), the triple, liquid–vapour–heater contact line recedes slower than the bubble foot edge (figure 1), so a thin liquid layer is trapped between the heated wall and the interface of the bubble. This layer of liquid is known as the microlayer. It was indirectly observed for the first time by Moore & Mesler (1961), whose micrometric homemade thermocouples measured high surface temperature variations with relatively long time periods, which could not be explained either by liquid advection or by evaporation in the contact line vicinity. Later, Torikai (1967) successfully performed its direct observation from below. They used a transparent electro-conductive glass as a heated wall, and noticed a dry area smaller than the bubble foot, which confirmed the existence of a liquid layer below the bubble. Jawurek (1969) was the first to measure its thickness with laser interferometry (LI) at a few μm. The microlayer plays a crucial role, as its low thickness leads to high heat transfer from the wall to the fluid, thereby efficiently cooling down the wall and considerably (up to $\sim$50 %) contributing to the overall bubble growth (Myers *et al.* 2005; Jung & Kim 2014; Yabuki & Nakabeppu 2014; Tecchio *et al.* 2024*a*).

The wettability of the wall, together with its natural heterogeneity and roughness can provide preferential places that act as the vapour bubble nucleation sites (Gallo *et al.* 2023). From the experimental point of view, the main parameter dependent on all these surface properties is the wall superheating ΔT (i.e. the difference of the wall temperature T_w and saturation temperature T_{sat} defined for the system pressure) required for the bubble nucleation. One calls it alternatively the nucleation barrier or the superheating of the nucleation site activation that results in the onset of nucleate boiling. For this reason, it is denoted ΔT_{ONB}. It is important to mention that the nucleation is controlled by the wall superheating and not by the wall heat flux.

To correctly target the growing bubble with cameras and sensors, the place of its nucleation should be fixed. The targeting is done either by localised heating or by creating a cavity that plays the role of an artificial nucleation site. This latter method was pioneered by Howell & Siegel (1966). Since then it has become a common practice used at present by almost all research groups working on boiling (Qi & Klausner 2005; Hutter *et al.* 2013; Kangude & Srivastava 2020; Voulgaropoulos *et al.* 2022; Zupančič *et al.* 2022). Shoji & Takagi (2001) investigated the boiling features of artificial cavities with conical, cylindrical and re-entrant geometries. They have found that cylindrical cavities provided the most stable ebullition cycles, which are the cycles of bubble growth and departure on the same site (Tong & Tang 2018). Such a behaviour was also found numerically by Whiting *et al.* (2024). They concluded that it resulted from the minimum bubble base radius prior to departure being constant and equal to the cavity radius, whereas this was not necessarily true for conical cavities.

The microlayer observation is difficult because, in addition to a small length scale, the time scale of the microlayer formation is of the order of several milliseconds for water at

https://doi.org/10.1017/jfm.2026.11566 Published online by Cambridge University Press

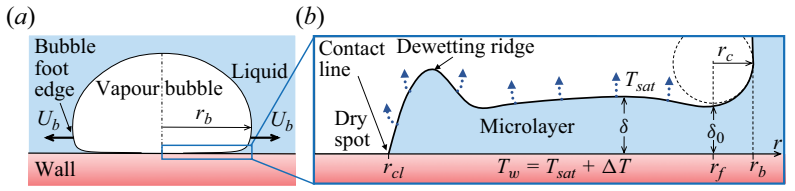


Figure 1. Schematics of a single bubble growing on a heated wall. (*a*) Bubble macroscopic view. (*b*) Microlayer.

atmospheric pressure. Since the 1960s, the microlayer observation and measurement by two simultaneously applied experimental methods (typically, the sidewise shadowgraphy and observation or measurement from below) remained the state of the art for a long time. Jung & Kim (2014) were first to apply a triple observation by adding to the optical observations from the side and a simultaneous observation with an infra-red (IR) camera from below, i.e. by using IR thermography (IRT). This gave access to understanding of the spatial distribution of heat and mass transfer along the microlayer. The technique of LI has long been used for the measurements of the microlayer thickness. Tecchio *et al.* (2024*c*) were first to apply the triple observation by replacing LI with white light interferometry (WLI).

The model of Cooper & Lloyd (1969) (cf. § 3.6 below) dominated theoretical ideas about the microlayer's formation until recently. It was based on the scaling of the microlayer thickness with that of the viscous boundary layer. It thus resulted in a monotonic growth of the microlayer thickness in agreement with its early experimental studies (Jawurek 1969; Koffman & Plesset 1983; Yabuki & Nakabeppu 2014). Such a picture was widely accepted by the scientific community until Chen, Haginiwa & Utaka (2017) discovered that the microlayer can have a bumped shape also observed in the forthcoming studies of other groups (Jung & Kim 2018; Narayan & Srivastava 2021; Tecchio *et al.* 2024*c*).

Following the initial idea of Zijl & Moalem-Maron (1978), it was shown experimentally (Tecchio *et al.* 2024*c*) that the formation of microlayer is analogous to the deposition of a thin liquid film on a flat plate that one pulls out vertically from a pool of liquid with a speed U_b. This phenomenon was first modelled by Landau & Levich (1942), who demonstrated that the thickness of such a film is defined by the interplay of the viscous and surface tension forces. According to their theory developed in the asymptotic limit $Ca_b \ll 1$

$$\delta_0 = 1.34 r_c Ca_b^{2/3}, \tag{1.1}$$

where the capillary number is $Ca_b = \mu U_b/\sigma$; μ and σ stand for the dynamic viscosity and the surface tension, respectively and r_c is the radius of liquid surface curvature near the plate. The same formula was rederived by Bretherton (1961) for the case of a film deposited by the receding meniscus inside a capillary. The microlayer is left behind the bubble foot edge of the curvature r_c^{-1} (figure 1*b*) receding with the speed $U_b = \dot{r}_b$ that represents the speed of bubble lateral growth (dot indicates the time derivative). This means that the microlayer thickness is controlled only by the viscous and surface tension forces while the overall bubble shape is controlled by the interplay of the liquid inertia and surface tension during the microlayer formation.

Two last columns of table 1 show the maximum values Ca_b^{max} and Re^{max} of the capillary and the Reynolds microlayer numbers $Re = U_b \rho_l \delta_0/\mu$, where ρ_l stands for the liquid density. They use the maximum U_b and δ_0 encountered during the computation of microlayer parameters in § 3.5. The values of $Re^{max} \simeq 20$ show some contribution of inertia at the bubble foot edge. However, as the velocity decreases exponentially with

https://doi.org/10.1017/jfm.2026.11566 Published online by Cambridge University Press

Case	Surface state	d (µm)	h (µm)	β (°)	q_a'' (kW m^{-2})	ΔT_{ONB} (K)	Ca_b^{max}	Re^{max}
A	No cavity	—	—	—	1100	31.5	6.6×10^{-3}	32.2
					64.6	16.1	5.7×10^{-3}	25.9
					71	15.3	6.1×10^{-3}	25.7
B	Cavity	38.6	70.5	6.7	80.7	15.7	6.2×10^{-3}	27
					90.4	16.0	4.7×10^{-3}	19.4
					103	16.5	—	—
					107	16.4	—	—
C	Cavity	26.7	52.9	4.6	200	9.2	4.2×10^{-3}	9.4

Table 1. List of different experiments. Cases A–C correspond to different boiling surfaces. Cases A and C refer to our previous works (Tecchio *et al.* 2024*b*,*c*). The maximum values of Ca_b and Re are not shown for 103 and 107 kW m^{-2} because the WLI fringes do not have high enough optical contrast to post-process the images.

decreasing r according to Bretherton (1961), the lubrication approximation should apply to the microlayer description.

The initial microlayer thickness $\delta_0(r)$ is that right after microlayer formation. One should note that the r_c value is much smaller than the bubble radius r_b shown in figure 1(*a*). This high curvature occurs in a transition zone between the nearly flat microlayer and the remaining nearly hemispherical part of the bubble interface. While Ca_b is accessible experimentally, it is unfortunately impossible to measure r_c by optical shadowgraphy because of the mirage effect that deforms the bubble image near the heated wall (Cooper 1983). It was previously shown (Tecchio *et al.* 2024*c*) that an assumption of a constant r_c/r_b ratio throughout the inertial stage gives results coherent with experiment and numerical simulation.

In this work, we aim to study in depth the bubble dynamics in saturated pool boiling experiments of water at atmospheric pressure by focusing on the microlayer formation. For this purpose, we investigate the single-bubble boiling regime (where one bubble grows without any influence from the others) with fast, synchronised and highly spatially resolved shadowgraphy coupled with WLI and IRT. Artificial nucleation centres are used as a means to produce different bubble growth rates by controlling the nucleation barrier, which allows us to investigate the initial microlayer thickness over a wide range of Ca_b. We develop a method to recover r_c from the experimental data and discuss the initial microlayer thickness for different cases; our data are finally compared with existing phenomenological models.

2. Experimental

A schematic of the experimental installation is presented in figure 2. The boiling cell consists of a water pool surrounded by a temperature-regulated jacket. The water pool is at atmospheric pressure and saturation temperature. The ultra-pure water (Merck Millipore) with 2 ppb total organic carbon and 18.2 MΩ cm resistivity, additionally purified *in situ* by the Milli-Q IQ 7003 installation, was used in all the experiments. The water was boiled for several hours prior to the experiments to eliminate the non-condensable gases.

2.1. *Boiling surfaces*

The boiling surfaces consist of a 3 mm-thick magnesium fluoride (MgF_2) porthole on which a 950 nm-thick indium-tin oxide (ITO) film is deposited by using a radio-frequency

https://doi.org/10.1017/jfm.2026.11566 Published online by Cambridge University Press

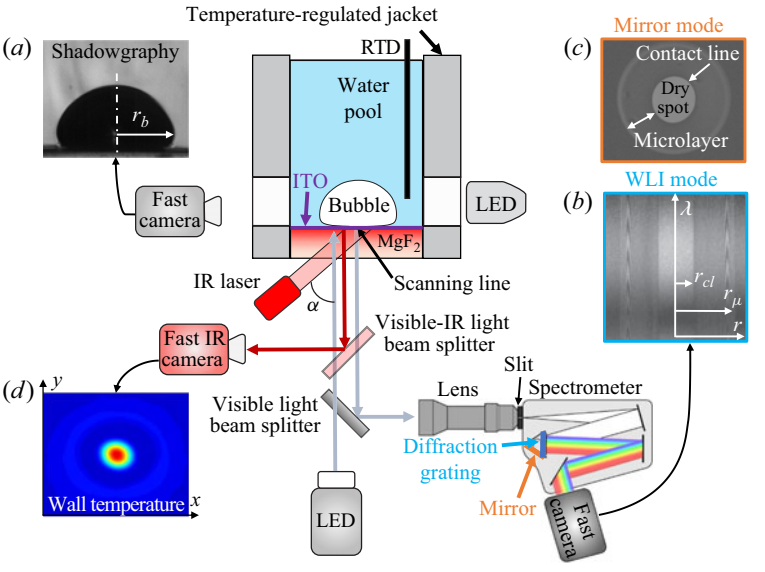


Figure 2. Schematics of the experimental set-up and experimentally obtained images. The sidewise shadowgraphy gives the overall bubble shape and its radius $r_b(t)$ (image (*a*)). The white-light interferometry (image (*b*)) gives the contact line radius $r_{cl}(t)$, the microlayer edge position $r_\mu(t)$ and the microlayer thickness $\delta(r, t)$. The mirror mode (image (*c*)) is used to check whether a bubble is axisymmetric and to align the slit with the bubble centre. The IRT gives the wall temperature distribution $T_w(x, y, t)$ (image (*d*)).

magnetron sputtering system. The MgF_2 is transparent to both visible and IR waves, whereas ITO is transparent in visible but opaque in the IR wavelength range. To ensure the growth of a single bubble at a time, the ITO film is heated up locally with an IR continuous laser (wavelength of 1.2 µm). The laser beam has a Gaussian-like profile. The applied wall heat flux q''_a is calculated as described in Appendix A. The heat flux can be varied among different experimental cases (see table 1) by changing the beam diameter and the laser power.

This study compares the data obtained from three different boiling surfaces; table 1 summarises their parameters. Case A refers to our previous work (Tecchio *et al.* 2024*a*,*c*), in which no artificial cavity was created on a boiling surface. The optically smooth ITO surface (its roughness was $\simeq$ 10 nm) had a 'natural' point defect that served as a nucleation site for the bubbles (figure 3*a*).

In cases B and C (the latter refers to the work of Tecchio *et al.* 2024*b*), the bubble nucleates on an artificial cavity with a depth h approximately twice larger than its upper diameter d (figure 3*c*). The cavity is fabricated on the MgF_2 window by the focused ion beam (FIB) technology prior to the ITO deposition. The cavity is slightly conical, with the slant angle β (figure 3*b*). However, it is quite small, so the cavity shape is close to cylindrical. The cavity parameters are provided in table 1.

The precise position of a cavity on the ITO is known *a priori* only approximately. To locate it precisely, one displaces the IR laser spot that is easily visible on the IRT image along the surface with the micrometric translation stage. Once the laser beam centre is close enough to the cavity, bubble nucleation occurs. Next, the laser beam is centred on the cavity. The natural defect in case A was localised with a similar procedure.

https://doi.org/10.1017/jfm.2026.11566 Published online by Cambridge University Press

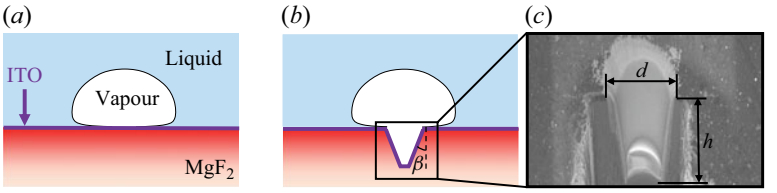


Figure 3. Schematics of the boiling surfaces. (*a*) No artificial cavity (case A of table 1). (*b*) Artificial cavity, cases B and C (the cavity is not to scale). (*c*) Slanted scanning electron microscopy image of the cavity. The substrate cross-cut is performed with FIB. The lengths h and d stand for the depth and the mouth diameter of a cavity, respectively.

2.2. *Measurement techniques*

The measurement techniques employed in this study are described extensively in our previous studies (Tecchio *et al.* 2024*b*,*c*). Only a concise description is given here. The bubble macroscopic shape and its radius $r_b(t)$ (figure 2*a*) are obtained by sidewise shadowgraphy with a spatial resolution of 32 μm px^{-1} for case A and 9 μm px^{-1} for cases B and C thanks to a better optical set-up.

The microlayer thickness is measured by WLI that has many advantages over LI. (i) The WLI is much more precise: for each r, the amount of data is comparable to the vertical image size in pixels in WLI, while it is one in LI (single laser wavelength). (ii) The spatial resolution of WLI is much larger. In LI, the distance between the measurement points is limited by the distance between the fringes. In WLI, it is limited only by the resolution of the optical system. (iii) The LI relies on the fringe number. When the vapour-liquid (V-L) interface slope is high (typically, near the edge of the measured r interval, e.g. near the contact line) the fringes become dense and some of them can be lost because of insufficient resolution of the optical system. So the LI results on a microlayer might be given only within a constant offset thickness. The WLI is deprived of such an uncertainty and always gives the absolute thickness value. (iv) The general shape of the microlayer corresponds to the WLI fringe shape (figure 2*b*) so the microlayer bump can be seen during the experiment without any processing.

The WLI is set up as follows. A LED light source produces a collimated beam of white light that is shone towards the bubble from below perpendicularly to the wall. The reflected light is directed with a visible light beam splitter towards a spectrometer. A slit located at the entrance of the spectrometer defines the scanning line, along which the microlayer profile is measured. The set-up is adjusted in such a way that the scanning line passes through the bubble centre. In the spectrometer, the light is dispersed by a diffraction grating; a fast camera records the spectral fringe map (figure 2*b*). It results from the interference of the rays reflected from the interfaces between MgF_2/ITO, ITO/microlayer and microlayer/vapour. In figure 2(*b*), the ordinate corresponds to the wavelength λ and the abscissa to the physical position along the scanning line. The diffraction grating can be replaced by a mirror to observe the bubble from below (figure 2*c*). These images serve to verify that, in all of the cases, the bubbles are nearly cylindrically symmetric thanks to a good quality of ITO (sufficiently smooth and chemically homogeneous). This allows us to associate the coordinate along the scanning line with the radial coordinate r. The microlayer thickness profile $\delta(r, t)$ is determined by comparing the experimental spectral intensity with the two-beam interference model (Tecchio 2022).

From figure 2(*b*), one can also obtain the dry spot (contact line) radius r_{cl} as the radius where the optical contrast changes sharply due to a difference of reflectivity (given by the Fresnel coefficients) from the interfaces of ITO with the vapour and the liquid that have

https://doi.org/10.1017/jfm.2026.11566 Published online by Cambridge University Press

r_{cl}, r_{μ}	± 0.08 mm
r_b	± 0.1 mm
δ	± 15 nm
ΔT	± 0.5 K

Table 2. Measurement uncertainties.

different refraction indices. From the optical analysis, one can also deduce the microlayer edge position r_{μ} as a maximal radial coordinate, within which the interference fringes appear. Even if the optical resolution is not high enough to distinguish them (which is often the case near the microlayer edge), they lead to a brighter image than the bulk liquid.

The wavelength bandwidth of WLI is 444.6–587.7 nm, and the spectral resolution is 0.21 nm px^{-1}. The WLI spatial resolution along r is 14 µm px^{-1} for case A and 7.9 µm px^{-1} for cases B, C thanks to a camera with a smaller pixel size. The spatial resolution defines the maximum measurable slope of the V-L interface (Tecchio *et al.* 2024*c*). The maximal slopes at $\lambda = 500$ nm are 0.38° for case A and 0.76° for cases B, C.

The IRT is used to measure the temporal evolution of the wall temperature distribution $T_w(x, y, t)$ in the Cartesian reference frame (x, y) (figure 2*d*). We use a homemade multilayer visible–IR light beam splitter (transparent to visible but reflective to IR) positioned between the boiling cell and the visible light beam splitter to reflect the IR light emitted by the ITO. The reflected IR radiation is captured by a fast IR camera in the range 3–5 µm. The recorded intensity is then related to temperature using a pixel-wise calibration (Schweikert, Sielaff & Stephan 2021). A resistance temperature detector (RTD in figure 2) measures the water pool temperature near the boiling surface. The temperature measurements for the calibration are taken with the liquid pool at thermally homogeneous conditions. The spatial resolution of the IR camera is 84 µm px^{-1} for cases A and C, and 100 µm px^{-1} for case B.

All optical observations are recorded synchronously at 4000 frames per second. Both the calibration and validation of WLI and IRT are described by Tecchio (2022) and the measurement uncertainties are provided in table 2.

3. Results and discussion

Table 1 shows the experimental cases that correspond to different boiling surfaces described above. The surfaces A and C were studied at a fixed heat power. Experiments in case B were performed for several heating power values corresponding to the reference heat fluxes 64–107 kW m^{-2}.

3.1. *Ebullition cycles*

Figure 4 depicts the temporal evolution of the wall superheating at the nucleation site location denoted ΔT_0. Figure 4(*a*) shows consecutive ebullition cycles. They follow a periodic pattern with a period t_c, which is a cycle duration. The high repeatability occurs thanks to a high quality of the boiling surface causing the nucleation on the single nucleation site, thus avoiding thermal and hydrodynamic interactions with other bubbles. This means that one ebullition cycle is sufficient to be studied as it is representative of the whole dynamics.

One can see that ΔT_0 periodically attains its maximum at a specific superheating. The maximum is reached at the bubble nucleation, where a sharp temperature drop occurs due

https://doi.org/10.1017/jfm.2026.11566 Published online by Cambridge University Press

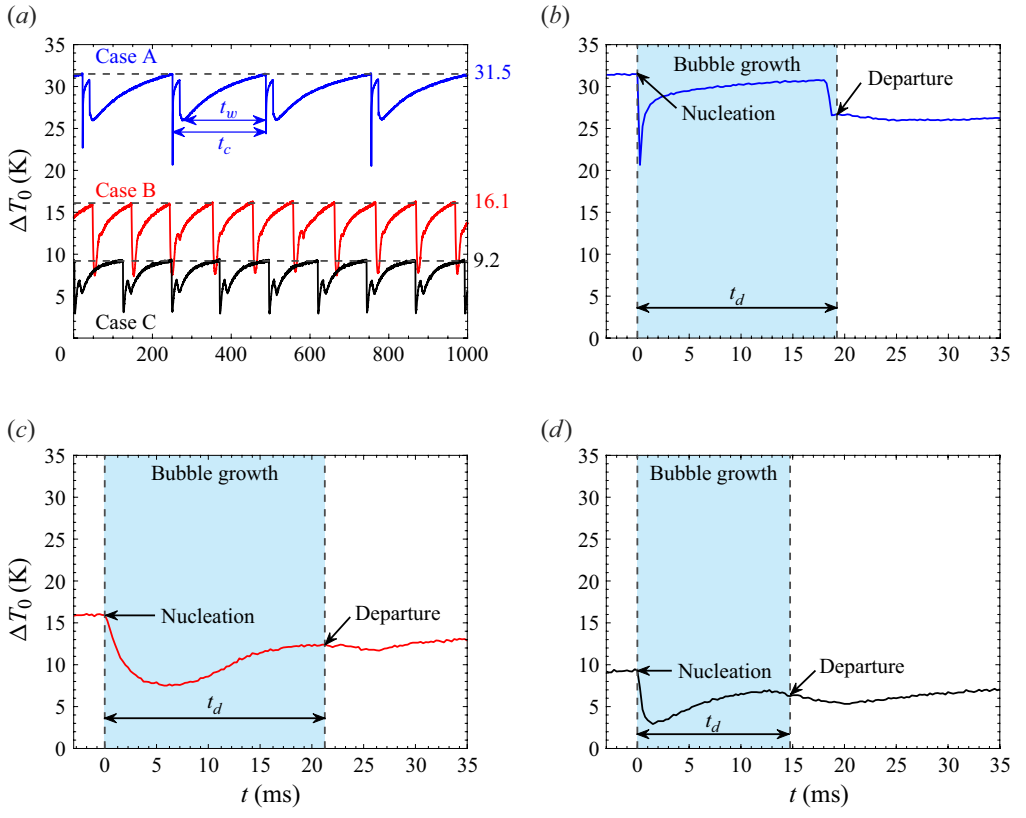


Figure 4. Wall superheating ΔT_0 measured at the nucleation site location as a function of time for the cases listed in table 1. The case B curves are given for $q''_a = 80.7\ \mathrm{kW\ m^{-2}}$. The time t in figures 4(*b–d*) is counted from the bubble inception. (*a*) Long-time evolution. The respective ΔT_{ONB} values are indicated to the right of each curve in K. (*b*) Evolution during the bubble growth time for case A (Tecchio *et al.* 2024*a*). (*c*) Evolution during the bubble growth time for case B. (*d*) Evolution during the bubble growth time for case C (Tecchio *et al.* 2024*b*).

to a consumption of energy needed to compensate the latent heat of vaporisation. The maximum superheating corresponds to ΔT_{ONB}. One can see (table 1) that it depends on the boiling surface and is smaller by factors 2 and 3.4 for cases B and C, respectively, in comparison with case A. Such a behaviour is non-monotonic with respect to the cavity diameter, which suggests that the relevant nucleation length scale is different (probably corresponding to the roughness inside the cavity). It is well known that controlling nucleation by the surface geometry is extremely difficult (Qi & Klausner 2005). Therefore, ΔT_{ONB} is used hereafter as a main parameter describing the boiling surface.

The detailed analysis of an ebullition cycle shows that it consists of the time t_d of the bubble residence on the heater and waiting time $t_w \gg t_d$ until next nucleation event, i.e. $t_c = t_d + t_w$ (cf. figure 4). The ΔT_0 evolution during the residence is analysed in figure 4(*b–d*). From now on, we set the time origin $t = 0$ at the bubble inception (nucleation) to describe a single ebullition cycle. The time evolution of ΔT_0 is qualitatively similar for all three cases. Once the nucleation occurs at $\Delta T_0 = \Delta T_{ONB}$, the temperature decreases because of a strong consumption of the latent heat at the fast inertial growth stage. Next, the temperature increases due to formation and growth of a dry spot at the

https://doi.org/10.1017/jfm.2026.11566 Published online by Cambridge University Press

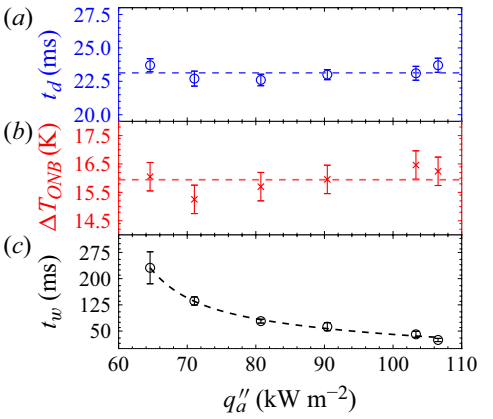


Figure 5. Impact of q''_a on (*a*) t_d, (*b*) ΔT_{ONB} and (*c*) t_w for case B. The lines are the eye guides.

nucleation site because the heat transfer to the vapour is very small. Although a dry spot forms immediately (cf. figure 8 below), ΔT_0 continues to decrease for some time. This can be attributed to a high evaporation in the contact line vicinity (Nikolayev 2022) that drains the energy stored in the wall. Next, the contact line evaporation manifests itself once again, when the advancing contact line approaches the bubble centre (just before the bubble departure under the action of buoyancy) causing a ΔT_0 decrease. It becomes more pronounced after the bubble departure due to the wall quenching by convection from the bulk colder liquid (Wei *et al.* 2025).

In case A, the ΔT_0 drop after nucleation is much sharper than in cases B and C because of a higher cooling rate due to evaporation, whose rate increases with ΔT_{ONB}. After the initial decrease, ΔT_0 increases because of the dry spot growth, which is also faster at a higher superheating (Zhang & Nikolayev 2022). The ΔT_0 decrease just before the bubble departure is sharper too because the contact line cooling effect increases with the local superheating.

3.2. *Effect of heat flux on the bubble growth*

Before considering in detail the effect of ΔT_{ONB} on the bubble dynamics, we discuss the effect of the applied heat flux q''_a. It is controlled by both the beam diameter D and the power of the IR laser q_{las} that can be varied independently and significantly (Appendix A). To evaluate the heat flux effect, we compare the bubble evolution observed at a fixed D and varying q_{las}. This is done for the boiling surface of case B, i.e. for the original data obtained in this work.

The influence of the applied heat flux q''_a on ΔT_{ONB}, the bubble growth time t_d and the waiting time t_w is analysed in figure 5, where the error bars of t_d and t_w are computed as a standard deviation over at least 7 ebullition cycles, and those for ΔT_{ONB} are the measurement uncertainties (these ΔT_{ONB} values are also shown in table 1). Here, ΔT_{ONB} stays nearly constant, regardless of q''_a. This indicates that the nucleation depends on the wall temperature but not on the wall heat flux, which is coherent both with the classical nucleation theory (Tong & Tang 2018) and the contemporary picture of nucleation (Gallo *et al.* 2023). No significant variation of the departure time t_d is detected either. However, t_w decreases with increasing q''_a. This occurs because ΔT_{ONB} is reached faster (the substrate is heated faster) when a higher heat flux is applied.

https://doi.org/10.1017/jfm.2026.11566 Published online by Cambridge University Press

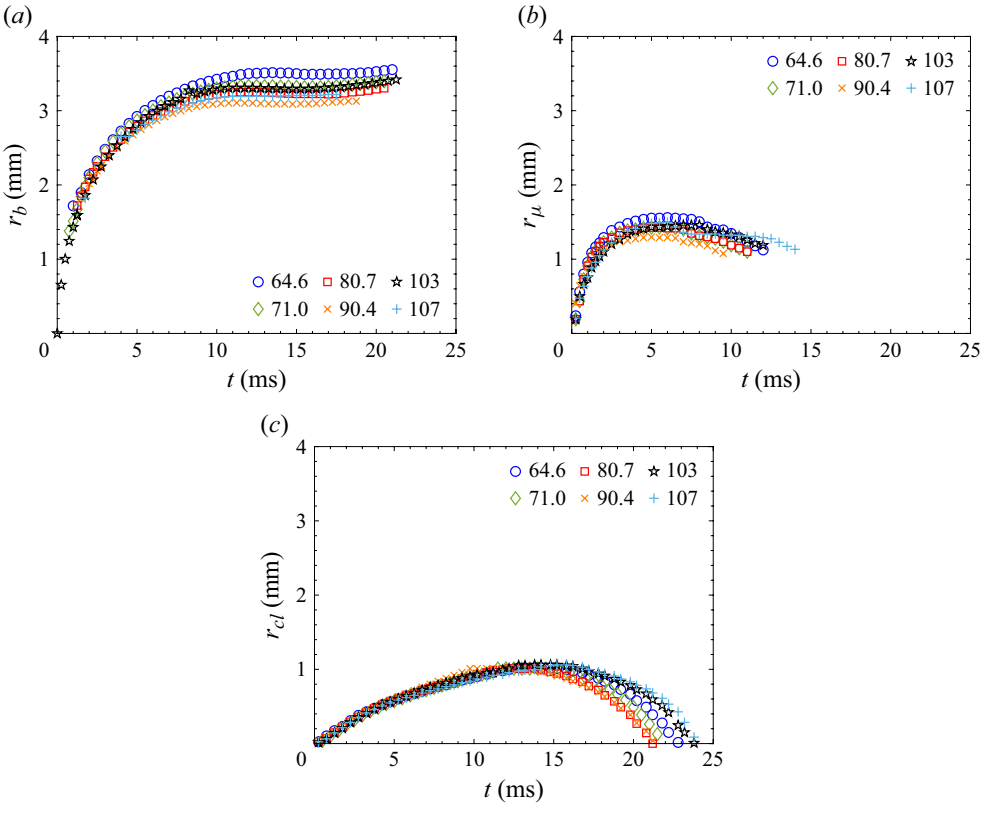


Figure 6. Time evolution of characteristic bubble radii for case B. The curve parameter is q_a'' in kW m^{-2}. The data are plotted from the bubble inception ($t = 0$) up to its departure from the wall. (*a*) Bubble radius r_b. (*b*) Microlayer edge position r_μ. (*c*) Contact line position r_{cl}.

It should be mentioned that the working interval of q_a'' is strongly limited for each boiling surface. On one hand, a certain flux value is necessary to achieve ΔT_{ONB}. For a smaller flux, the wall superheating is smaller, i.e. the nucleation does not occur. This is the well-known 'onset of boiling' phenomenon; the corresponding flux value is given by the boiling curve (Tong & Tang 2018). On the other hand, the single-bubble regime (meaning the growth of a bubble independently of the others) does not exist above a certain q_a'' value. Because of the decrease of t_w with q_a'' (figure 5*c*), the bubble that previously departed from the heater coalesces with the bubble that grows on the heater (Hutter *et al.* 2013). The latter bubble cannot thus be considered as independent of the others any more.

Figure 6 depicts the time evolution of the main geometrical parameters during bubble growth: the bubble radius r_b, the microlayer edge radius r_μ and the dry spot (i.e. contact line) radius r_{cl}. In figure 6(*a*), the missing r_b data are explained by the presence of a tiny nearly stationary bubble that obscures the growing bubble in the shadowgraphy optical path for the few first measurement points, except for $q_a'' = 103$ kW m^{-2}. This stationary bubble is situated far away from the nucleation site (because it is invisible by both WLI and IRT) and thus does not disturb the boiling dynamics. Note that the bubble inception can be accurately found with the WLI images, which allows us to determine the $t = 0$ point for the r_b graph and thus accurately calculate U_b at the inertial stage.

Evidently, the early bubble growth stages are similar for all the q_a'' values. Slight dispersion can be observed in the late stages (after the inertial growth phase), mostly within

https://doi.org/10.1017/jfm.2026.11566 Published online by Cambridge University Press

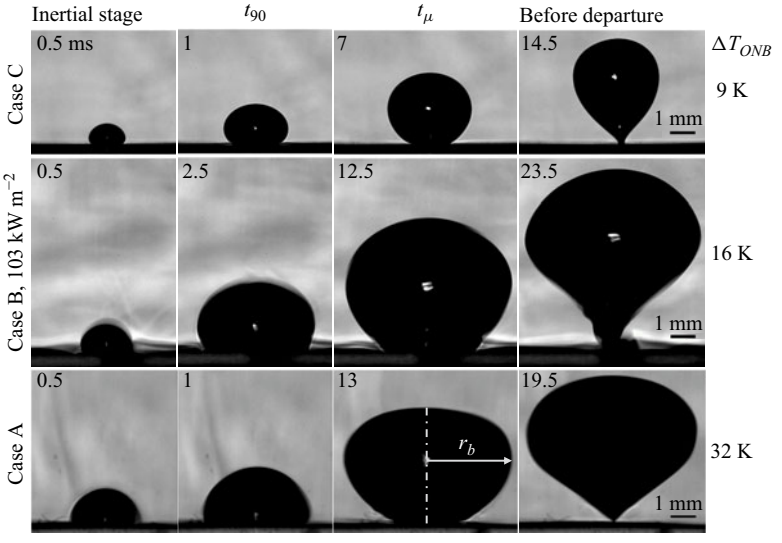


Figure 7. Shadowgraphy bubble images at key time moments for different cases. Number on each image corresponds to time t in ms counted from the bubble inception.

the statistical dispersion observed between consecutive ebullition cycles and without a clear dependence on q''_a. Together with figure 5(a), these data show that the bubble growth dynamics is independent of the applied heat flux, at least on the inertial stage.

This quite peculiar feature is explained by both the single-bubble regime and the massive heater. Consider these aspects separately. For the massive heater case, a bubble uses for its growth, occurring during t_d, the energy that was previously stored in the heater (Tecchio *et al.* 2024*a*) during $t_w \gg t_d$. The accumulated energy is much larger than that supplied by the heating source, at least during the inertial stage, i.e. the time t_{90}, cf. Appendix B. The situation with thin foil heaters (Zupančič *et al.* 2022) is expected to be different. Unlike single-bubble boiling, in the multiple-bubble boiling experiment, there is a dependence on the heat flux due to the thermal interaction between the nucleation sites controlling the activation of neighbouring sites (Marie *et al.* 2022). As new sites are activated at a larger local superheating ΔT_0, this situation corresponds to a larger effective ΔT_{ONB} in the single-bubble boiling. Therefore, the key parameter to study the bubble growth dynamics for the single-bubble boiling (and, in particular, its inertial stage that controls the microlayer formation) is the nucleation barrier ΔT_{ONB}.

3.3. *Bubble growth dynamics*

Figure 7 depicts the macroscopic bubble shape evolution. The corresponding curves for the bubble (r_b), microlayer (r_μ) and contact line (r_{cl}) radii are plotted in figure 8. The bubble radius grows rapidly during the early, inertia-driven growth stage. The bubble shape is hemispherical here (cf. the first column of figure 7) due to the action of the inertial forces caused by the rapid bubble expansion. A thin liquid layer (microlayer) forms between the bubble and the heater because r_μ grows faster than r_{cl}. The microlayer formation threshold is analogous to the dynamic wetting transition observed in capillaries (Gao *et al.* 2018; Zhang & Nikolayev 2023), where the contact line cannot follow a receding liquid meniscus. The microlayer thus extends from the contact line to the bubble edge so its radial length is $r_\mu - r_{cl}$. This is the microlayer bubble growth regime according to the classification of Bureš & Sato (2021). After a rapid inertial stage, the r_μ growth slows

https://doi.org/10.1017/jfm.2026.11566 Published online by Cambridge University Press

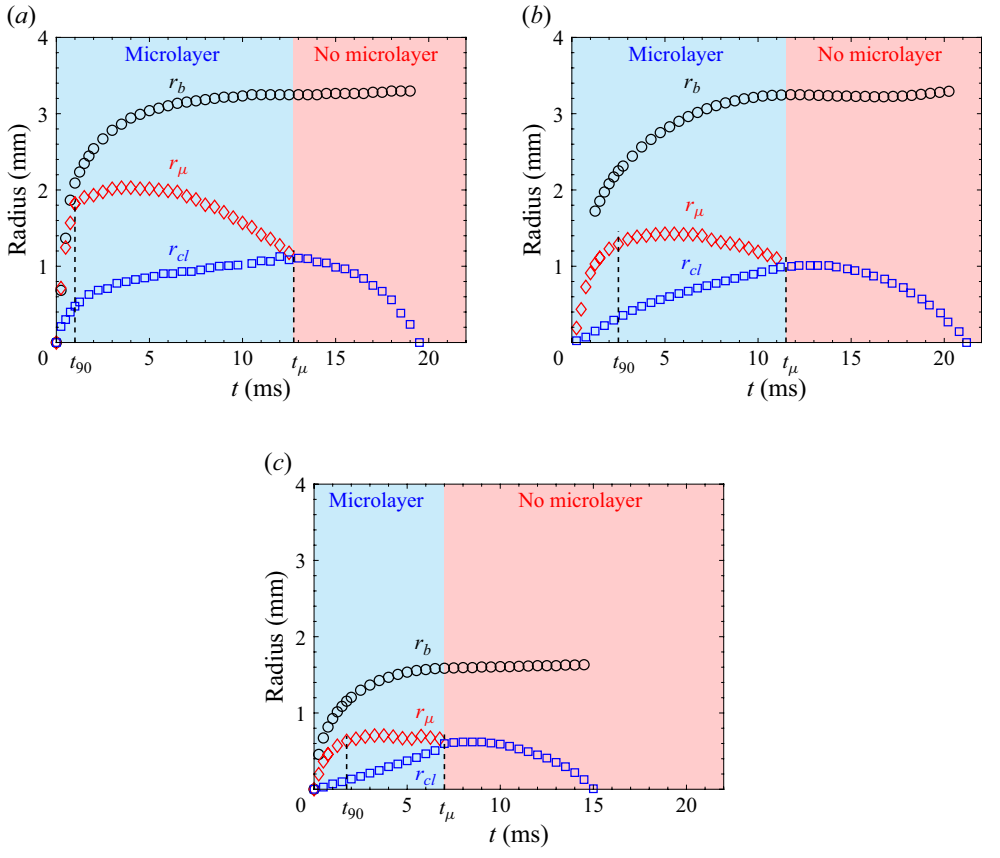


Figure 8. Time evolution of bubble radii during bubble growth on the heated wall for different cases. Here, r_b is the bubble radius, r_μ is the microlayer edge position and r_{cl} is the dry spot (contact line) radius. The data are plotted from the bubble inception ($t = 0$) up to its departure from the wall. (*a*) Case A (Tecchio *et al.* 2024*a*). (*b*) Case B for $q''_a = 80.7\,\mathrm{kW\,m^{-2}}$. (*c*) Case C (Tecchio *et al.* 2024*b*).

down and crosses over to the thermal diffusion-controlled growth regime, which occurs loosely at the time $t = t_{90}$ where 90 % of microlayer is formed, cf. figure 8. The bubble takes a progressively more spherical shape under the action of the surface tension, which is shown in the second column of figure 7; r_b reaches a slow (heat transfer-controlled) growth stage. The radius r_μ starts decreasing while the contact line keeps receding (i.e. r_{cl} grows). This lasts until $t = t_\mu$, where the condition $r_\mu = r_{cl}$ is satisfied (i.e. microlayer disappears) and r_{cl} attains its maximum. The contact line bubble growth regime (Bureš & Sato 2021) starts. The corresponding bubble shapes are displayed in the third column of figure 7. Depending on the surface quality, the contact line can be pinned on surface defects for a short time close to t_μ (r_{cl} remains constant). Note that tiny defects do exist in spite of a high surface quality. After depinning, the contact line starts advancing back to the bubble centre (i.e. r_{cl} decreases) under the action of buoyancy forces that eventually cause the bubble departure from the heater at $t = t_d$. The bubble images just before departure are shown in the last column of figure 7. The bubble growth dynamics observed here is similar to earlier experiments (Jung & Kim 2014).

As discussed in § 3.2, cases A–C mainly differ by the value of ΔT_{ONB}. A comparison of the growth dynamics for different ΔT_{ONB} (figure 8 is replotted in Appendix C) clearly

https://doi.org/10.1017/jfm.2026.11566 Published online by Cambridge University Press

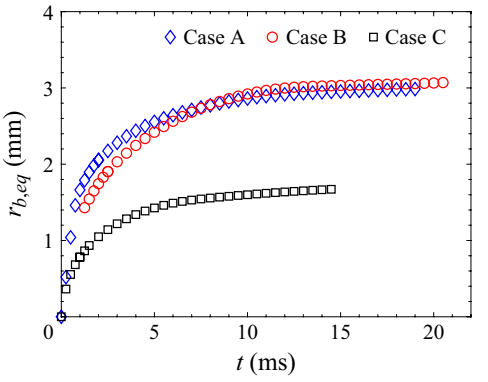


Figure 9. Equivalent bubble radius for different boiling surfaces. In case B, $q''_a = 80.7\ \mathrm{kW\ m^{-2}}$. The data are plotted from the bubble inception ($t = 0$) up to its departure from the wall.

shows two features. First, the r_b growth rate during initial inertial stage (i.e. U_b) increases with ΔT_{ONB}. Second, both r_μ and r_{cl} are larger for a larger ΔT_{ONB}. Larger values of both U_b and r_μ are explained by a faster growth at the inertial stage and thus stronger inertial forces causing the hemispherical bubble shape mentioned above. This is coherent with recent microlayer simulations (Zhang *et al.* 2025). A faster r_{cl} growth (i.e. a faster heater dewetting) is a consequence of a larger local superheating (Zhang & Nikolayev 2022).

A similar tendency is observed in figure 9, where the equivalent bubble radius $r_{b,eq}$ (that of a sphere of the same volume V_b as the bubble) is plotted as a function of time t for cases A–C. The slope increases with ΔT_{ONB} at the early inertial stage of the bubble growth.

3.4. *Microlayer dynamics*

Figure 10(*a*) depicts an example of the evolution of the microlayer profile measured with WLI. Recent numerical simulations (Urbano *et al.* 2018; Giustini 2024; Saini *et al.* 2024; Tecchio *et al.* 2024*c*) show that the microlayer consists of two parts: a dewetting ridge near the contact line followed by a nearly flat part, as illustrated in figure 1(*b*). All the results on microlayer thickness presented below correspond to this flatter part because the ridge features inaccessibly high slopes. We remind the reader that only its part where the interface slope is smaller than the maximum observable slope (§ 2.2) can be measured by interferometry (Tecchio *et al.* 2024*a*; Choi & Kim 2025).

One can observe three main features. First, the observable radial length of the microlayer grows at early times ($t \leqslant 3.75$ ms). Second, the microlayer exhibits a maximum thickness discussed later on. Third, the microlayer thins over time. Two phenomena can cause the microlayer thinning: its evaporation and a radial liquid flow. Because of the strong viscous stresses present in the thin liquid film, the flow exists only near the bubble edge and the contact line. Therefore, the radial flow in the measurable central part of microlayer can be neglected (Zhang & Nikolayev 2021). The validity of this assumption is evaluated *a posteriori* in Appendix D. The thinning occurs due to evaporation only, which is confirmed by figure 10(*a*), where the microlayer profile is shifted vertically, almost without any other modification. A similar behaviour is observed for cases A and C (Tecchio *et al.* 2024*b*,*c*).

Thanks to the microlayer thinness, one can assume a quasi-stationary and linear temperature profile in the vertical direction. By neglecting the heat flux towards the vapour, one can combine the energy and mass balances for a fixed r, which results

https://doi.org/10.1017/jfm.2026.11566 Published online by Cambridge University Press

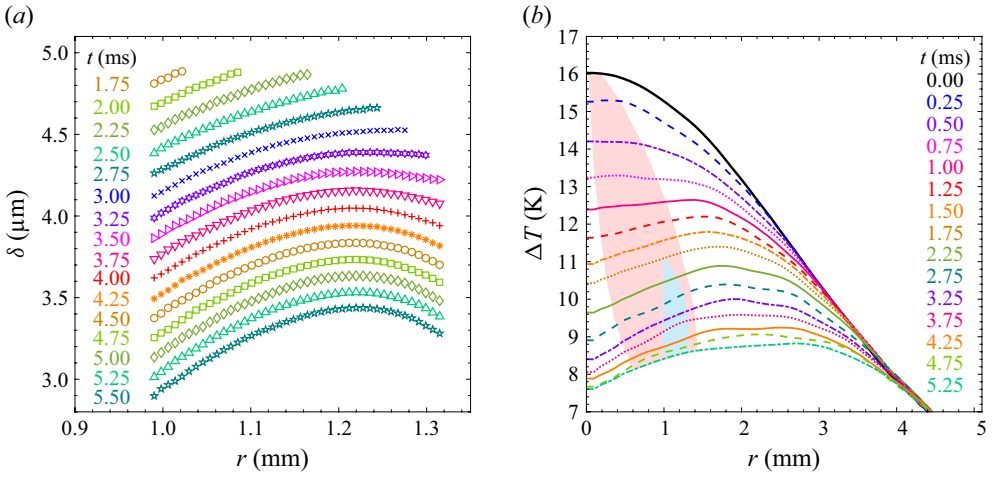


Figure 10. Spatio-temporal variation of δ and ΔT for case B for $q''_a = 80.7\,\mathrm{kW\,m^{-2}}$. (*a*) Microlayer profile $\delta(r, t)$. (*b*) Superheating $\Delta T(r, t)$.

(Tecchio *et al.* 2024*a*) in the thickness evolution equation

$$\rho_l \dot{\delta} = -\frac{\Delta T}{\mathcal{L}(\delta/k_l + R^i)}, \tag{3.1}$$

where k_l stands for the liquid thermal conductivity, and R^i represents the interfacial thermal resistance (cf. Appendix E).

Figure 10(*b*) illustrates the spatio-temporal evolution of ΔT used in (3.1). The blue shading indicates the extent of the observable part of the microlayer, i.e. the fringes (compare with the envelope of figure 10*a*). The red shading indicates the microlayer total extent $[r_{cl}, r_\mu]$, cf. § 3.3. The value of ΔT initially experiences a very fast decrease. It causes such a rapid motion of the bubble interface (for $t < 1.75$ ms in the case of figure 10*b*) that the fringes are smeared and are almost indistinguishable: the camera shutter speed becomes a limiting factor. This graph shows that it is possible to measure approximately 30 % of the microlayer extent at the end of its formation, which is much larger than in our preceding work on case A (Tecchio *et al.* 2024*c*) thanks to the improvement of installation, cf. § 2.2.

3.5. *Initial microlayer thickness*

We describe hereafter the postprocessing of experimental data to obtain the initial microlayer thickness δ_0, i.e. the thickness that the microlayer would have without evaporation (§ 1). Next, we discuss the reconstruction of δ_0 and justify the model validity by checking its coherence with other data.

When U_b varies in time, so does δ_0. One can speak of microlayer formation because there is no radial flow and the thickness would remain constant once the film is created if evaporation were absent. According to the above δ_0 definition

$$\delta_0(r) = \delta(r, t = t_f), \tag{3.2}$$

where t_f is the time moment at which the film is formed at a distance r from the bubble centre; t_f is a function of r. One can define an inverse to $t_f(r)$ function defining the point $r = r_f(t)$ where the thickness given by (1.1) is formed at time t. Therefore, any

https://doi.org/10.1017/jfm.2026.11566 Published online by Cambridge University Press

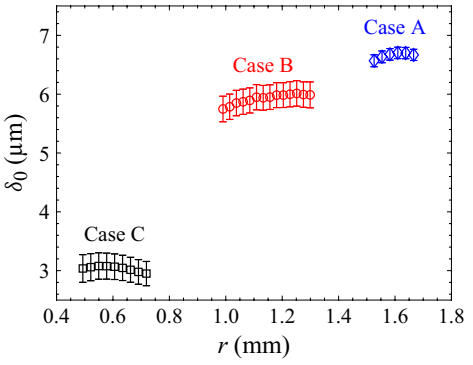


Figure 11. Initial microlayer thickness as a function of the radial position r for different cases. For case B, $q''_a = 80.7\ \mathrm{kW\ m^{-2}}$.

variable related to the microlayer formation can be defined as a function of either t or r. The film formation (i.e. deposition) inside a capillary thanks to a meniscus receding with a variable speed was numerically analysed by Zhang & Nikolayev (2021). It was shown that r_f does not correspond to the position of the meniscus apex but is shifted inward by its radius of curvature. In the growing bubble case, the position of the meniscus apex is analogous to r_b, whereas the radius of curvature, to that of the bubble foot edge r_c (cf. figure 1*b*), which leads to

$$r_f \simeq r_b - r_c. \tag{3.3}$$

To obtain $\delta_0(r)$, previous approaches (Utaka, Kashiwabara & Ozaki 2013; Yabuki & Nakabeppu 2014; Jung & Kim 2018) used the data for the first thickness measurement obtained right after microlayer formation at the point r. We denote the time of this first measurement as $t_m(r)$. For instance, considering the data set presented in figure 10(*a*), $t_m(r = 1\ \mathrm{mm}) = 1.75$ ms but $t_m(r = 1.1\ \mathrm{mm}) = 2.25$ ms simply because the microlayer is formed at $r = 1.1$ mm later than at $r = 1$ mm. However, the choice $\delta_0(r) = \delta(r, t_m)$ made in the above works would be inaccurate in our case where the initial superheating is large so the microlayer evaporation is quick. To reconstruct $\delta_0(r)$ from $\delta(r, t_m)$, one can use (3.1). However, the R^i value is *a priori* unknown. Nonetheless, we know that $R^i \ll \delta/k_l$ right after the microlayer formation (Tecchio *et al.* 2024*a*) (cf. Appendix E). Therefore, for simplicity, R^i is neglected in (3.1) within the time interval $[t_f, t_m]$. The analytical solution of (3.1) can then be readily obtained

$$\delta_0(r) = \sqrt{\delta(r, t_m(r))^2 + \frac{2k_l}{\mathcal{L}\rho_l}[t_m(r) - t_f(r)]\overline{\Delta T}(r)}, \tag{3.4}$$

where $\overline{\Delta T}$ is the average over $[t_f, t_m]$ superheating. We verified that the averaging is applicable in such a small time interval. The initial microlayer thickness δ_0, the radius of interface curvature at the bubble edge r_c and the time of microlayer formation t_f can now be recovered at each point r by solving a set of three equations (1.1), (3.3), (3.4) that has a unique solution, cf. Appendix F.

Figure 11 shows δ_0 for cases A–C, corresponding to progressively decreasing ΔT_{ONB} (cf. table 1). One can see immediately that a higher ΔT_{ONB} implies a thicker microlayer and a larger microlayer extent. This can be explained if one mentions that a faster bubble growth (that occurs at a larger ΔT_{ONB}, cf. figure 8), causes a higher capillary number Ca_b (figure 12*a*) resulting in a higher δ_0 according to (1.1).

https://doi.org/10.1017/jfm.2026.11566 Published online by Cambridge University Press

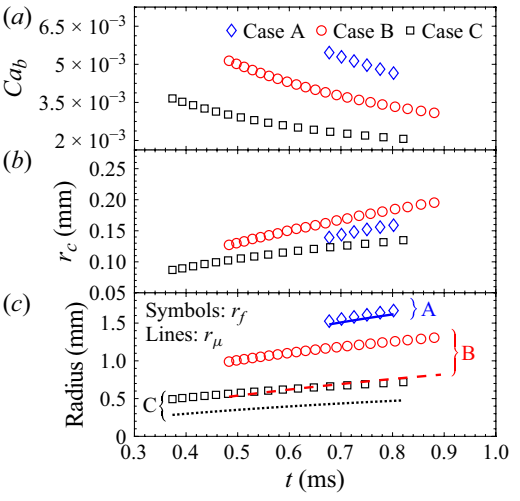


Figure 12. The parameters Ca_b (*a*), r_c (*b*) and r_f (*c*) at the instant of microlayer formation as functions of time for different cases. Here, $r_\mu(t)$ from figure 8 is shown for comparison in (*c*). For case B, $q''_a = 80.7\ \mathrm{kW\ m^{-2}}$.

The increase of both the extent of the microlayer and the position of its maximum with ΔT_{ONB} can also be explained by considering Ca_b. Its larger value at a higher ΔT_{ONB} causes a faster r_f growth (figure 12*c*) because larger inertial forces cause a stronger bubble flattening, thus promoting its rapid radial expansion (figure 7, 8) and microlayer formation. These experimental observations are in line with recent numerical simulations of the hydrodynamics of microlayer formation (Zhang *et al.* 2025).

In figure 11, one notices that the microlayer shows a 'bumpy' profile for all cases. The bump was also observed by other groups (Chen *et al.* 2017; Jung & Kim 2018). This bump occurs simply because r_c grows while Ca_b decreases with time, as shown in figure 12. Because of this, (1.1) predicts a point of maximum thickness in the microlayer profile (Tecchio *et al.* 2024*c*).

In figure 12, one mentions that all the quantities related to the microlayer formation are defined for quite small times. In other words, $t_f(r)$ is quite short with respect to the bubble growth time for all r (which becomes evident when considering plotting a function inverse to that of figure 12*c*). In general, this occurs because the microlayer is formed during a short inertial stage. One should also note that the microlayer thickness can be measured only within a short spatial range (for figure 10*a*, between 1 and 1.3 mm, which corresponds to the range of r_f) limited by the optical resolution of WLI. In figure 6(*a*), one can see that r_b takes only 0.4 ms to sweep the measurable microlayer part, which corresponds to the time range in figure 12.

In figure 12(*c*), the microlayer formation distance r_f is compared with r_μ that was previously called the microlayer edge position. Both quantities characterise the microlayer length. However, r_f comes from the microlayer physics, while r_μ is defined by the numerical aperture of the optical system (see § 2). Note that r_f is always larger than r_μ but smaller than r_b, which shows the internal coherency of the model. In cases A and C, r_μ and r_f are very close to each other while their difference is quite large for case B.

In figure 12(*b*), a non-monotonic variation of r_c with ΔT_{ONB} is apparent. One would naïvely expect that r_c for case B is smaller than for case A, which is not the case. However, to gain insight into the overall bubble shape, the ratio r_c/r_b matters, not the r_c value. In figure 13, the monotonicity of r_c/r_b is evident. Moreover, this ratio is nearly constant

https://doi.org/10.1017/jfm.2026.11566 Published online by Cambridge University Press

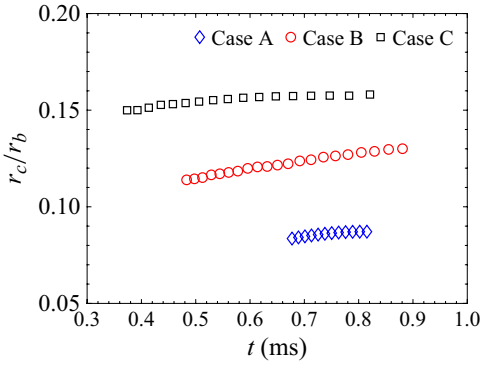


Figure 13. The ratios r_c/r_b at microlayer formation as functions of time for different cases. For case B, $q_a'' = 80.7\,\mathrm{kW\,m^{-2}}$.

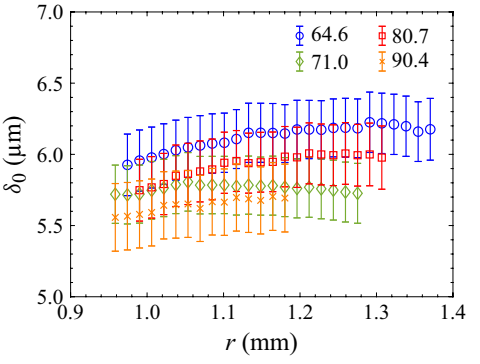


Figure 14. Effect of q_a'' (parameter of the curves in $\mathrm{kW\,m^{-2}}$) on δ_0 for case B. The data for 103 and $107\,\mathrm{kW\,m^{-2}}$ are not shown because the WLI fringes do not have high enough optical contrast to post-process the images.

over time, which indicates that bubble shapes during the inertial stage can be considered homothetic, which suggests a self-similar bubble dynamics. This result corroborates the assumption about the constant value of r_c/r_b made earlier (Tecchio *et al.* 2024*c*). One can see that the ratio decreases with ΔT_{ONB}, which is explained by the bubble flattening by inertial forces during microlayer formation (see figure 7).

Note that $r_c(t) \ll r_b(t)$ so $r_f(t) \approx r_b(t)$, according to (3.3). This means that the assumption $r_f(t) = r_b(t)$ implicitly made by Tecchio *et al.* (2024*c*) was reasonable.

The internal coherence of the above method of recovery of the microlayer parameters needs to be verified. One of the coherency criteria is the monotonicity of the $r_f(t)$ function that should be satisfied since the microlayer should be formed farther away from the bubble centre at a later time as the bubble foot edge recedes. Indeed, the resulting $r_f(t)$ is a monotonically increasing function for each of the cases. This was not, however, imposed in the starting equations (1.1), (3.3), (3.4). Moreover, since the equations involve a non-monotonic function $\delta(r, t_m)$, the monotonicity of $r_f(t)$ is not *a priori* guaranteed. It holds, however. Another coherency criterion is the monotonic variation of the resulting parameters with ΔT_{ONB}. Such a coherency shows that the above model correctly describes the microlayer formation.

https://doi.org/10.1017/jfm.2026.11566 Published online by Cambridge University Press

The effect of the heat flux on δ_0 is shown in figure 14. All cases have a similar δ_0 magnitude and a similar radial position of its maximum. As the heat flux does not affect the bubble inertial stage considerably, this is an expected result.

A slight δ_0 variation between the cases can be explained by small variations of Ca_b (cf. also figure 6). Here, r_c remains within the uncertainty ($\pm 70\,\mu$m found by propagating the uncertainties of table 2). One observes a non-monotonic microlayer profile attaining a maximum of δ at $r \approx 1 - 1.3$ mm. This study shows once again (§ 3.2) the insensitivity of the microlayer dynamics to the applied heat flux.

3.6. *Comparison with previous microlayer models*

First, we compare our data with the model of Cooper & Lloyd (1969). It is still widely used (Jung & Kim 2018; Qi, Li & Li 2025) and results in a formula $\delta_0 = A\sqrt{\nu t_f}$, where $\nu = \mu/\rho_l$ is the kinematic viscosity and A is a dimensionless constant. In figure 15(*a*), our data are fitted with the above law (with t_f calculated as specified in § 3.5) to determine the A value. It results in 0.452, 0.424 and 0.233 for cases A, B, C, respectively, which is of the same order of magnitude as the 0.8 proposed by Cooper & Lloyd. These values are, however, much larger than the 0.035 of Jung & Kim (2018) and much smaller than the 2.87 used by Qi *et al.* (2025). Without surprise, the fit is very poor. Evidently, the above equation cannot describe a bump of $\delta_0(r)$ shape as $t_f(r)$ is always a monotonically increasing function, whatever the method of its determination.

In a recent paper, Zhang, El Mellas & Magnini (2024) proposed a theoretical model for the initial microlayer thickness based on the Landau–Levich mechanism of microlayer formation. It is the only one that accounts for the key role of surface tension. It does not contain any adjustable parameters. To determine r_c needed to find δ_0 with (1.1), the key issue is the liquid pressure p_l near the bubble foot edge. The curvature r_c^{-1} can then be defined as a pressure difference with the vapour (i.e. system) pressure divided by σ according to the Laplace law. Zhang *et al.* postulated that the $p_l(r)$ expression is given by the Rayleigh theory describing the growth of a spherical vapour bubble in the infinite inviscid liquid, i.e. for $r \geqslant r_b$. Not only do they apply this expression to the much more complex geometry of figure 1, but they extrapolate it to $r < r_b$, i.e. inside the microlayer, where the shear stress is important.

To obtain δ_0 from their theory, we used our experimental $r_b(t)$ values of figure 8 in the equations ((2.14), (2.15), (2.17), (2.18)) of Zhang *et al.*. The result is compared in figure 15(*b*) with our data. While the order of magnitude given by the Zhang *et al.* model is good, there is a non-negligible quantitative deviation (up to 80 % in case C). Moreover, the predicted microlayer thickness is larger in case B than in case A, which is contrary to the trend observed; the inertial forces are larger in case A because of a much higher bubble growth rate and should thus result in a larger thickness. More details on the comparison can be found in Appendix G.

4. Conclusion

In this work, we investigate the dynamics of the single-bubble growth at nucleate boiling of water. Our focus is on the physics of microlayer formation and its evaporation. The experiments were performed at atmospheric pressure. In order to understand the physical phenomena of microlayer formation under a wide range of bubble growth rates, we study different boiling surfaces by creating an artificial cavity of micrometric size in some of them. All of them are of very good quality, producing periodic ebullition cycles and axisymmetric bubbles, which show a good surface quality and are convenient for future comparisons with numerical simulations.

https://doi.org/10.1017/jfm.2026.11566 Published online by Cambridge University Press

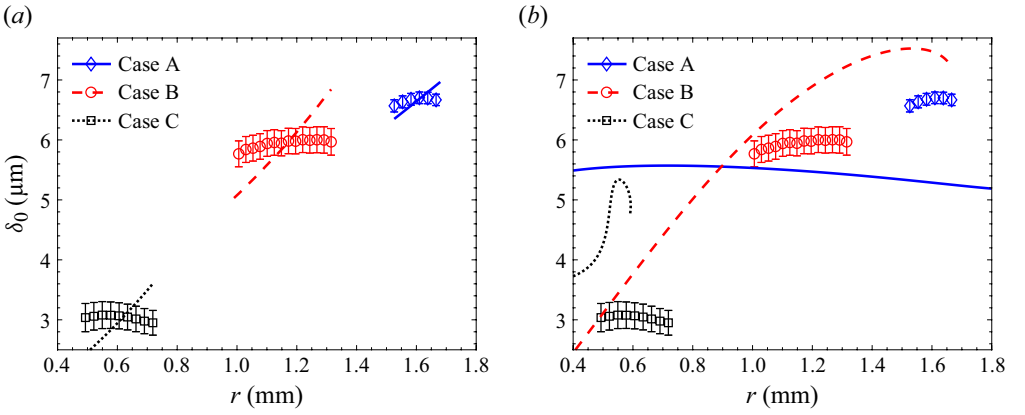


Figure 15. Comparison of our data from figure 11 on the initial microlayer thickness (characters with added error bars) with predictions of previous phenomenological models (lines). (*a*) Comparison with the Cooper & Lloyd (1969) model. (*b*) Comparison with the Zhang *et al.* (2024) model.

It is found that the applied heat flux has almost no effect on the bubble growth. The superheating at which bubble inception occurs (i.e. that of onset of nucleate boiling, also called a nucleation barrier), the time of bubble residence on the heater and the time evolution of the bubble characteristic sizes, including those of the microlayer and dry spot, are nearly insensitive to the heat flux. Only the waiting time depends on it. We argue that such a behaviour is specific to boiling with a single nucleation site on a massive heater.

Three cases differing by the nucleation barrier are compared. The results show that the use of an artificial cavity can reduce the nucleation barrier by a factor of three. We show that the bubble growth rate during the early (inertia-controlled) stage increases with the nucleation barrier. This has a strong effect on the microlayer (both its area and thickness increase) and thus on the overall bubble dynamics.

The microlayer disappearance occurs through vanishing of its area, and not of its thickness. Therefore, the term 'microlayer depletion' often used in the literature is not appropriate.

By further developing the microlayer formation theory that uses an analogy with the deposition of Landau–Levich films, we propose a new model. It provides a method of reconstruction, from the experimental data, of several key parameters like the time moment of the microlayer formation at a given distance from the bubble centre, the curvature of the bubble foot edge and the initial microlayer thickness. In all the cases, the initial microlayer thickness features a bumped profile observed previously by our and several other groups. The results show that the initial thickness of the microlayer, its area and the position of its maximum increase with the nucleation barrier. The radius of curvature of the bubble foot edge (i.e. that of the bubble interface close to the heater) is a key quantity in the Landau–Levich theory but is difficult to access experimentally. During the early (inertial) stage of the bubble growth, it increases proportionally to the bubble radius, suggesting that the bubble growth remains self-similar. All the reconstructed microlayer parameters show a monotonic behaviour with the nucleation barrier and are physically coherent. This shows the validity of the microlayer model based on the Landau–Levich theory. The microlayer physics should remain the same for all the fluids and operating conditions as far as the Reynolds and capillary microlayer numbers remain small; however, specific parameters (microlayer occurrence, length, shape and dynamics) should depend not only on the above conditions but also on the surface state.

https://doi.org/10.1017/jfm.2026.11566 Published online by Cambridge University Press

Case	q_a'' (kW m^{-2})	q_{las} (W)	α (°)	D (mm)	$\mathcal{A}$	q_a (W)
A	1100	4.1	32	1.5	0.47	1.94
	64.6	4.6	—	—	—	2
	71	5	—	—	—	2.2
B	80.7	5.8	20	6.3	0.44	2.6
	90.4	6.5	—	—	—	2.9
	103	7.3	—	—	—	3.2
	107	7.5	—	—	—	3.3
C	200	2	43	2.5	0.49	0.98

Table 3. Parameters characterising the experimental cases. Here, q_{las}, α, $\mathcal{A}$ and q_a stand for the output laser radiant power, the angle of incidence, the ITO absorbance and the wall absorbed power, respectively.

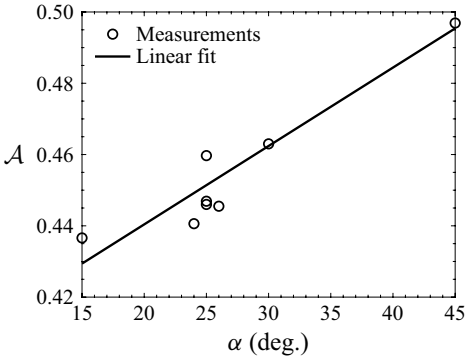


Figure 16. The IR absorbance $\mathcal{A}$ of the ITO measured (Tecchio 2022) as a function of is the angle of incidence α. The line shows the linear regression $\mathcal{A} = 0.0022\alpha + 0.3964$.

A comparison with two existing phenomenological theories of microlayer initial thickness has been carried out. The Cooper & Lloyd (1969) equation is unable to explain our results. The model of Zhang *et al.* (2024) gives a qualitative agreement with the microlayer shape and a generally reasonable thickness magnitude. It, however, lacks precision: the predicted by it microlayer thickness can differ as strongly as 80 % from the actual value.

Acknowledgements. The authors are grateful to V. Padilla (SPEC, CEA Paris-Saclay) for technical assistance.

Declaration of interests. The authors report no conflict of interest.

Appendix A. The IR laser parameters and applied heat flux

The ITO heating can be characterised by several parameters controlled in the experiment. They are shown in table 3. First is the total laser power q_{las} of the incident wave. It is known from the laser electrical current given by the device itself and a calibration with the powermeter. The distribution of the IR laser intensity is a Gaussian-like function of the radial distance from the beam axis. The beam hits the ITO film with the angle of

https://doi.org/10.1017/jfm.2026.11566 Published online by Cambridge University Press

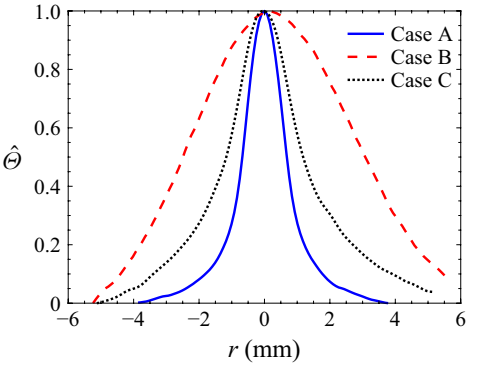


Figure 17. Dimensionless temperature profiles along the scanning line for different values of ΔT_{ONB}. For case B, $q_a'' = 80.7\,\mathrm{kW\,m^{-2}}$.

incidence α (figure 2). Since it is different from zero, the heating power profile is slightly elliptical.

Only a part $q_a = \mathcal{A} q_{las}$ of the laser power is absorbed by ITO, where $\mathcal{A}$ is the IR absorbance. It depends on α (figure 16). The laser beam profile is characterised with its half-width D. To determine D and α, we consider the two-dimensional superheating temperature field $\Delta T(x, y)$ (figure 2*d*) measured with the IRT just before the nucleation event and define the dimensionless temperature $\hat{\Theta} = \Delta T(x, y)/\Delta T_{ONB}$. Then, we select the dimensionless isotherm $\hat{\Theta} = 1/\sqrt{2}$ and fit an ellipse to it. Here, D is determined as its minor diameter. The ellipticity gives α (Tecchio 2022) that, in its turn, defines the ITO absorbance $\mathcal{A}$ determined with the fit to the experimental data (figure 16). Then the heat flux $q_a'' = 4\mathcal{A} q_{las}/(\pi D^2)$ is determined. All the above parameters are given in table 3. This technique gives an estimate that is sufficient in our case because the flux is used only as a reference value. The profiles of $\hat{\Theta}$ just before the nucleation along the scanning line are depicted in figure 17. Note that the minor diameter lies at an angle to the scanning line, so D should not be evaluated with this figure.

Appendix B. Estimation of energy partition during the bubble growth

The following estimation helps to show that, in the present experiments, a major part of the energy used during the microlayer growth comes from that accumulated during the waiting time by the massive heater due to its high heat capacity. The energy needed to form a bubble during the microlayer growth time t_{90} can be estimated as $Q_b = \mathcal{L}\rho_v V_b$, where ρ_v is the vapour density that can be taken at saturation and $V_b = 4/3\pi r_{b,eq}^3$ can be evaluated at $t = t_{90}$ by using the data of figure 9, cf. table 4. This energy can be compared with that supplied by the IR laser during the microlayer growth $Q_a = q_a t_{90}$. The ratio Q_a/Q_b gives a strongly overestimated contribution of the laser power because the laser spot is larger than the microlayer area, so a large part of Q_a is spent to heat up the solid and the liquid.

Appendix C. Comparison of the bubble growth dynamics for cases A–C

The data of figures 6 and 8 are replotted in figure 18 (except for case B that is plotted for $q_a'' = 103\,\mathrm{kW\,m^{-2}}$ to show a different dataset) to reveal the dependence of the bubble

https://doi.org/10.1017/jfm.2026.11566 Published online by Cambridge University Press

Case	q_a'' (W m^{-2})	t_{90} (m s)	$r_{b,eq}$ (m m)	V_b (m m^3)	Q_b (m J)	q_a (W)	Q_a (m J)	Q_a/Q_b
A	1100	1	1.66	19.3	25.6	1.94	1.94	0.076
	64.6	2.5	1.95	30.8	41.1	2	5	0.122
	71	2.5	1.9	28.6	38.1	2.2	5.5	0.145
B	80.7	2.5	1.9	28.9	38.5	2.5	6.25	0.162
	90.4	2.25	1.76	23	30.6	2.8	6.3	0.206
	103	3.25	2.05	36	47.9	3.2	10.4	0.217
	107	3.25	2.06	36.7	48.8	3.3	10.725	0.22
C	200	1	1.56	16.1	21.4	0.98	0.98	0.044

Table 4. The values relevant to the estimation of the laser power contribution to the bubble growth. The time-dependent quantities ($r_{b,eq}$, V_b, Q_b, Q_a) are evaluated at $t = t_{90}$.

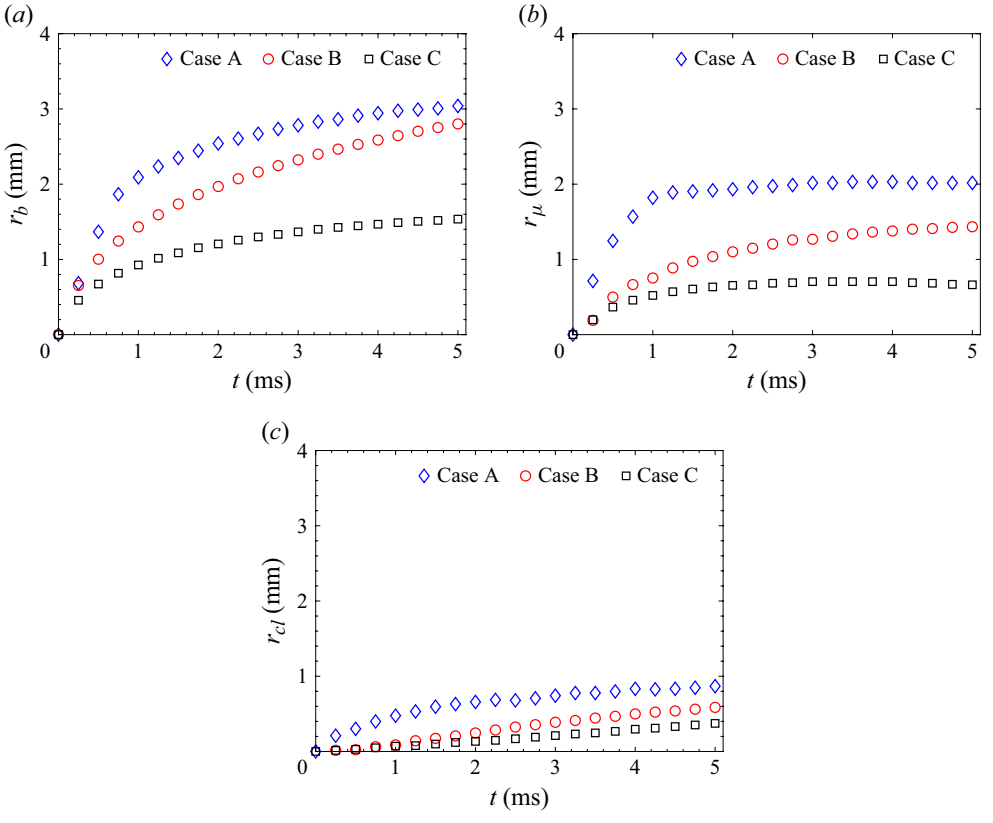


Figure 18. Time evolution of characteristic bubble radii for cases A–C. Case B is plotted for $q_a'' = 103$ kW m^{-2}. (*a*) Bubble radius r_b. (*b*) Microlayer edge position r_μ. (*c*) Contact line position r_{cl}.

growth dynamics on the nucleation barrier, which is different for cases A–C (table 1). Only the initial (mostly controlled by inertia) growth stage is shown. One can clearly see that both the increase speed and the magnitude of the quantities r_b, r_μ and r_{cl} grow from case C ($\Delta T_{ONB} = 9$ K) to case B ($\Delta T_{ONB} = 16$ K) and further on, to case A ($\Delta T_{ONB} = 32$ K). One concludes that the inertial stage is controlled by ΔT_{ONB}.

https://doi.org/10.1017/jfm.2026.11566 Published online by Cambridge University Press

Appendix D. Justification of the assumption of negligible radial flow

The pressure gradient in the microlayer can be evaluated as the capillary pressure σ/r_c at the bubble foot edge divided by the microlayer length, roughly r_b. This pressure gradient is balanced by the viscosity term of the Stokes equation, $\mu r_b/(\tau\delta^2)$, where r_b/τ is the radial flow speed, τ being the characteristic flow time scale. From this balance, $\tau = \mu r_b^2 r_c/(\sigma\delta^2) \simeq 30\,\text{ms}$, which is much larger than $t_f < 1\,\text{ms}$ so radial flow can be indeed neglected.

Another aspect of the radial flow concerns the Marangoni effect, i.e. the hydrodynamic stress induced by the surface tension gradient

$$\nabla\sigma = \frac{\mathrm{d}\sigma}{\mathrm{d}T}\nabla T^i \tag{D1}$$

induced by that of the interfacial temperature $T^i = T_{sat} + q''^i R^i$ appearing due to the interfacial thermal resistance R^i discussed in Appendix E. Here, q''^i is the interfacial heat flux

$$q''^i = \frac{k_l \Delta T}{\delta + k_l R^i}. \tag{D2}$$

One can see that ∇T^i can be estimated as $\nabla T_w \varrho/(1+\varrho)$, where $\varrho \simeq 0.35$ is defined in (E1). The gradient $|\nabla T_w| \simeq 1\,\text{K mm}^{-1}$ (figure 10*b*) leads to $|\nabla\sigma| \simeq 50\,\mu\text{Pa}$, which is much smaller than $\sigma/r_c \simeq 60\,\text{Pa}$ used for the estimation above (in the present case, $\mathrm{d}\sigma/\mathrm{d}T \approx -0.192\,\text{mN m}^{-1}\,\text{K}^{-1}$). This justifies the omission of the Marangoni effect in the microlayer theory.

Appendix E. Estimation of the impact of the interfacial thermal resistance on the reconstruction of the initial microlayer thickness

In § 3.5, the assumption $R^i \ll \delta/k_l$ has been made to recover an analytical formula (3.4) for δ_0. However, the R^i value at t_m can be found from (3.1) by using the values $\delta(t_m)$ and $\delta(t_m + 0.25\,\text{ms})$ (figure 10*a*) because the other parameters are known from the experiment; t_m definition is discussed in (§ 3.5). One finds that the ratio

$$\varrho = R^i k_l/\delta \tag{E1}$$

is approximately 0.1 and 0.15 for cases A and C, respectively. However, in case B, it can reach 0.35, in particular for $q''_a = 80.7\,\text{kW m}^{-2}$ (the 'worst' case). We evaluate here a deviation that we introduced in the main text by the zero R^i assumption.

In agreement with earlier findings of Tecchio *et al.* (2024*c*), we assume that R^i grows linearly in time starting at t_f from the value given by the linearised Schrage theory (Nikolayev 2022) with the unity accommodation coefficient

$$R^i_{theo} = \frac{T_{sat}\sqrt{2\pi R_v T_{sat}}(\rho_l - \rho_v)}{2\mathcal{L}^2\rho_l\rho_v}, \tag{E2}$$

where $\mathcal{L}$, $\mathcal{R}_g$ and ρ_v denote the latent heat, specific gas constant and the vapour density, respectively. This R^i value originates from the finiteness of the velocity of the vapour molecules leaving the liquid–vapour interface. One integrates (3.1) numerically backwards in time over the interval $[t_f, t_m]$ by using the experimental value of $\delta(t_m)$ as an initial condition. This equation is solved together with (1.1), (3.3) to recover δ_0, t_f and r_c.

https://doi.org/10.1017/jfm.2026.11566 Published online by Cambridge University Press

	$R^i = 0$	$R^i \neq 0$	Deviation, %
δ_0 (μm)	6.20	5.85	5.6
r_c (μm)	191	179	6.4
t_f (ms)	0.75	0.73	2.0

Table 5. The values of δ_0, r_c and t_f computed with and without R^i for case B and $q''_a = 80.7\ \mathrm{kW\ m^{-2}}$, $r = 1.17$ mm, corresponding to the highest deviations.

The effect of R^i on the is shown in table 5. One can notice that it corresponds to an overestimation of less than 7 % of the values of interest. We emphasise that this is the worst case; generally, the overestimation of δ_0 is less than 5 %.

Appendix F. Solution for δ_0, t_f and r_c and its uniqueness

The set (1.1), (3.3), (3.4) is solved for δ_0, t_f and r_c at each point r (that corresponds to the microlayer formation point r_f) with the following algorithm:

(i) initialise $r_c = 0$;
(ii) from (3.3), calculate r_b;
(iii) from the $r_b(t)$ curve, evaluate t_f as a time corresponding to r_b;
(iv) find the time average $\overline{\Delta T}(r)$ in the interval $[t_f, t_m]$;
(v) compute $\delta_0(r)$ from (3.4);
(vi) compute U_b as the $r_b(t)$ slope at $t = t_f$;
(vii) use both δ_0 and U_b to re-evaluate r_c with (1.1);
(viii) repeat steps (ii–vii) until r_c converges.

For all cases, ΔT spatial dependence is smoothed and linearly interpolated prior to the computation because WLI and IRT spatial resolutions differ so their data are not at the same points. Similarly, the smoothed fit of $r_b(t)$ is used. The convergence of such an algorithm is quite fast, only several iterations are necessary.

We analyse hereafter the uniqueness of the solution of the set (1.1), (3.3), (3.4). First, one can reduce it to a single equation with respect to t_f by excluding r_c from (1.1) with (3.3) and then substituting the resulting δ_0 into (3.4)

$$1.34(r_b - r)Ca_b^{2/3} = \sqrt{\delta(t_m)^2 + \frac{2k_l}{\mathcal{L}\rho_l}(t_m - t_f)\overline{\Delta T}}, \tag{F1}$$

where the fixed argument r is abandoned for brevity. Both sides of (F1) are plotted in figure 19 as functions of t_f. The dependence of the right-hand side on t_f is quite weak because, on one hand, $\Delta T(t)$ is weakly varying in the region where δ is measured (shaded in blue in figure 10*b*), and on the other, the second term is smaller than $\delta(t_m)^2$. For the left-hand side, the variation is stronger. As $r_b(t)$ monotonically grows but its derivative (i.e. $Ca_b(t)$) monotonically decreases, the product $r_b(t)Ca_b^{2/3}(t)$ exhibits a maximum, which explains a bump in the δ_0 shape (Tecchio *et al.* 2024*c*). However, a subtraction of $rCa_b^{2/3}(t)$ leads to a monotonically increasing behaviour. The intersection of the curves corresponding to both sides of (F1) is thus unique. A change in r induces a horizontal shifting of the whole right-hand side curve (note the red line in figure 19); the other effects

https://doi.org/10.1017/jfm.2026.11566 Published online by Cambridge University Press

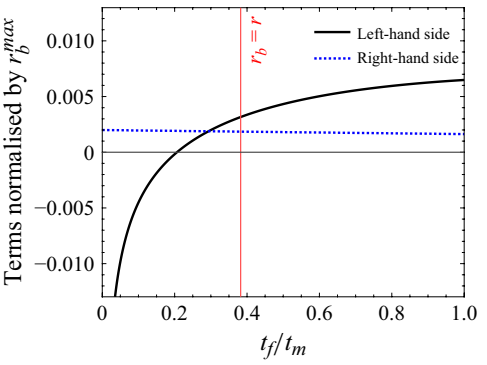


Figure 19. The variation of both sides (scaled by $r_b^{max} = 3.3$ mm) of (F1) with t_f/t_m. The graph is shown for case B ($q_a'' = 80.7\,\mathrm{kW\,m^{-2}}$) and $r = 1.3$ mm.

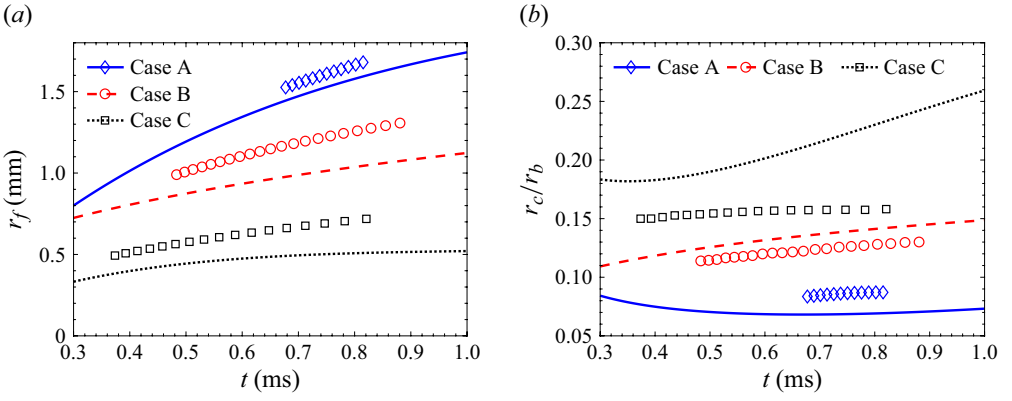


Figure 20. Comparison of the experimental data for different radii (symbols) with the respective predictions of Zhang *et al.* (2024) (lines). (*a*) Time evolution of r_f compared with that of the matching point denoted $\bar{x}$ by Zhang *et al.* (*b*) Time evolution of r_c/r_b.

of r on both sides are weak so the general trend remains the same. Once t_f is known, it is evident that a unique couple of δ_0 and r_c can be derived from it. The solution is thus unique for each r.

Appendix G. Details of comparison with the model of Zhang *et al.* (2024)

In addition to discussion in § 3.6, we present here more details on the comparison with the theoretical model of Zhang *et al.* (2024). The comparisons of our data from figures 12(*c*) and 13 are shown in figure 20. The model of Zhang *et al.* does not evaluate r_f. However, it is commensurate with the position of the matching point of the bubble foot edge and the microlayer (their $\bar{x}$). They are compared in figure 20(*a*). One can see that the values are quite close for each case and their behaviour is similar. The evolution of r_c/r_b is compared in figure 20(*b*). One can see that, while our data show that the bubble shape evolution is homothetic, this is not the case of the model of Zhang *et al.*, in particular for case C.

https://doi.org/10.1017/jfm.2026.11566 Published online by Cambridge University Press

References

Bretherton, F.P. 1961 The motion of long bubbles in tubes. *J. Fluid Mech.* **10**, 166–188.

Bureš, L. & Sato, Y. 2021 On the modelling of the transition between contact-line and microlayer evaporation regimes in nucleate boiling. *J. Fluid Mech.* **916**, A53.

Chen, Z., Haginiwa, A. & Utaka, Y. 2017 Detailed structure of microlayer in nucleate pool boiling for water measured by laser interferometric method. *Intl J. Heat Mass Transfer* **108**, 1285–1291.

Choi, J. & Kim, H. 2025 The influence of liquid vapor interface inclination on the microlayer profile reconstruction from interferometry fringe patterns in boiling bubbles. *Appl. Therm. Engng* **258**, 124733.

Cooper, M.G. 1983 The 'mirage' in boiling. *Intl J. Heat Mass Transfer* **26** (7), 1088–1090.

Cooper, M.G. & Lloyd, A.J.P. 1969 The microlayer in nucleate pool boiling. *Intl J. Heat Mass Transfer* **12**, 895–913.

Gallo, M., Magaletti, F., Georgoulas, A., Marengo, M., De Coninck, J. & Casciola, C.M. 2023 A nanoscale view of the origin of boiling and its dynamics. *Nat. Commun.* **14** (1), 6428.

Gao, P., Liu, A., Feng, J.J., Ding, H. & Lu, X.-Y. 2018 Forced dewetting in a capillary tube. *J. Fluid Mech.* **859**, 308–320.

Giustini, G. 2024 Hydrodynamic analysis of liquid microlayer formation in nucleate boiling of water. *Intl J. Multiphase Flow* **172**, 104718.

Howell, J.R. & Siegel, R. 1966 Incipience, growth, and detachment of boiling bubbles in saturated water from artificial nucleation sites of known geometry and size. In *3rd International Heat Transfer Conference*, pp. 12–23. Begellhouse.

Hutter, C., Sanna, A., Karayiannis, T.G., Kenning, D.B.R., Nelson, R.A., Sefiane, K. & Walton, A.J. 2013 Vertical coalescence during nucleate boiling from a single artificial cavity. *Exp. Therm. Fluid Sci.* **51**, 94–102.

Jawurek, H.H. 1969 Simultaneous determination of microlayer geometry and bubble growth in nucleate boiling. *Intl J. Heat Mass Transfer* **12** (8), 843–848.

Jung, S. & Kim, H. 2014 An experimental method to simultaneously measure the dynamics and heat transfer associated with a single bubble during nucleate boiling on a horizontal surface. *Intl J. Heat Mass Transfer* **73**, 365–375.

Jung, S. & Kim, H. 2018 Hydrodynamic formation of a microlayer underneath a boiling bubble. *Intl J. Heat Mass Transfer* **120**, 1229–1240.

Kangude, P. & Srivastava, A. 2020 Understanding the growth mechanism of single vapor bubble on a hydrophobic surface: experiments under nucleate pool boiling regime. *Intl J. Heat Mass Transfer* **154**, 119775.

Koffman, L.D. & Plesset, M.S. 1983 Experimental observations of the microlayer in vapor bubble growth on a heated solid. *J. Heat Transfer* **105**, 625–632.

Landau, L.D. & Levich, B.V. 1942 Dragging of a liquid by a moving plate. *Acta Physicochim. USSR* **17**, 42–54.

Marie, A., Cioulachtjian, S., Lips, S. & Sartre, V. 2022 Thermal interactions between nucleation sites and the solid wall during pool boiling of a pure fluid: a review. *Intl J. Therm. Sci.* **174**, 107388.

Moore, F.D. & Mesler, R.B. 1961 The measurement of rapid surface temperature fluctuations during nucleate boiling of water. *AIChE J.* **7** (4), 620–624.

Myers, J.G., Yerramilli, V.K., Hussey, S.W., Yee, G.F. & Kim, J. 2005 Time and space resolved wall temperature and heat flux measurements during nucleate boiling with constant heat flux boundary conditions. *Intl J. Heat Mass Transfer* **48**, 2429–2442.

Narayan, L.S. & Srivastava, A. 2021 On the identification and mapping of three distinct stages of single vapor bubble growth with the corresponding microlayer dynamics. *Intl J. Multiphase Flow* **142**, 103722.

Nikolayev, V.S. 2022 Evaporation effect on the contact angle and contact line dynamics. In *The Surface Wettability Effect on Phase Change* (ed. M. Marengo & J. De Coninck), chap. 6, pp. 133–187. Springer.

Qi, R.-S., Li, Y.-N. & Li, Z.-Y. 2025 A hydrodynamic model for the microlayer structure under heterogeneous bubbles in pool boiling. *Phys. Fluids* **37** (8), 087218.

Qi, Y. & Klausner, J.F. 2005 Heterogeneous nucleation with artificial cavities. *J. Heat Transfer* **127** (11), 1189–1196.

Saini, M., Chen, X., Zaleski, S. & Fuster, D. 2024 Direct numerical simulations of microlayer formation during heterogeneous bubble nucleation. *J. Fluid Mech.* **984**, A70.

Schweikert, K., Sielaff, A. & Stephan, P. 2021 Pixel-wise in situ calibration method for high accuracy infrared thermography of moving targets. *Infrared Phys. Technol.* **118**, 103862.

Shoji, M. & Takagi, Y. 2001 Bubbling features from a single artificial cavity. *Intl J. Heat Mass Transfer* **44**, 2763–2776.

https://doi.org/10.1017/jfm.2026.11566 Published online by Cambridge University Press

SNOEIJER, J.H., DELON, G., FERMIGIER, M. & ANDREOTTI, B. 2006 Avoided critical behavior in dynamically forced wetting. *Phys. Rev. Lett.* **96** (17), 174504.

TECCHIO, C. 2022 Experimental study of boiling: characterization of near-wall phenomena and bubble dynamics. PhD thesis, Université Paris-Saclay, France.

TECCHIO, C. *et al.* 2024*a* Microlayer evaporation during bubble growth in nucleate boiling. *Intl J. Heat Mass Transfer* **231**, 125860.

TECCHIO, C., REGOLI, I., CARITEAU, B., ZALCZER, G., ROCA I CABARROCAS, P., BULKIN, P., CHARLIAC, J., VASSANT, S. & NIKOLAYEV, V.S. 2024*b* Effect of an artificial cavity on the microlayer and contact line dynamics during bubble growth in nucleate boiling. *J. Phys.: Conf. Ser.* **2766** (1), 012121.

TECCHIO, C., ZHANG, X., CARITEAU, B., ZALCZER, G., ROCA I CABARROCAS, P., BULKIN, P., CHARLIAC, J., VASSANT, S. & NIKOLAYEV, V.S. 2024*c* Microlayer in nucleate boiling seen as Landau–Levich film with dewetting and evaporation. *J. Fluid Mech.* **989**, A4.

TONG, L.S. & TANG, Y.S. 2018 *Boiling Heat Transfer and Two-Phase Flow*, 2nd edn. CRC Press.

TORIKAI, K. 1967 Heat transfer in a contact area of a boiling bubble on a heating surface. *Bull. JSME* **10**, 338–348.

URBANO, A., TANGUY, S., HUBER, G. & COLIN, C. 2018 Direct numerical simulation of nucleate boiling in micro-layer regime. *Intl J. Heat Mass Transfer* **123**, 1128–1137.

UTAKA, Y., KASHIWABARA, Y. & OZAKI, M. 2013 Microlayer structure in nucleate boiling of water and ethanol at atmospheric pressure. *Intl J. Heat Mass Transfer* **57** (1), 222–230.

VOULGAROPOULOS, V., AGUIAR, G.M., MARKIDES, C.N. & BUCCI, M. 2022 Simultaneous laser-induced fluorescence, particle image velocimetry and infrared thermography for the investigation of the flow and heat transfer characteristics of nucleating vapour bubbles. *Intl J. Heat Mass Transfer* **187**, 122525.

WEI, L., BOIS, G., PANDEY, V. & NIKOLAYEV, V.S. 2025 Effect of contact line evaporation during nucleate boiling studied by multiscale numerical simulation. *Appl. Therm. Engng* **275**, 126690.

WHITING, M.S., VAN DEN BERGH, W.J., THEODORAKIS, P.E. & EVERTS, M. 2024 Influence of cavity geometry on the bubble dynamics of nucleate pool boiling. *Phys. Fluids* **36** (8), 087102.

YABUKI, T. & NAKABEPPU, O. 2014 Heat transfer mechanisms in isolated bubble boiling of water observed with MEMS sensor. *Intl J. Heat Mass Transfer* **76**, 286–297.

ZHANG, X., EL MELLAS, I., ANDREINI, N. & MAGNINI, M. 2025 The microlayer and force balance of bubbles growing on solid in nucleate boiling. *Intl J. Multiphase Flow* **183**, 105049.

ZHANG, X., EL MELLAS, I. & MAGNINI, M. 2024 Predicting initial microlayer thickness in nucleate boiling using Landau–Levich theory. *J. Fluid Mech.* **997**, A44.

ZHANG, X. & NIKOLAYEV, V.S. 2021 Liquid film dynamics with immobile contact line during meniscus oscillation. *J. Fluid Mech.* **923**, A4.

ZHANG, X. & NIKOLAYEV, V.S. 2022 Dewetting acceleration by evaporation. *J. Fluid Mech.* **948**, A49.

ZHANG, X. & NIKOLAYEV, V.S. 2023 Physics and modeling of liquid films in pulsating heat pipes. *Phys. Rev. Fluids* **8** (8), 084002.

ZIJL, W. & MOALEM-MARON, D. 1978 Formation and stability of a liquid microlayer in pool boiling and growth of a dry area. *Chem. Engng Sci.* **33** (10), 1331–1337.

ZUPANČIČ, M., GREGORČIČ, P., BUCCI, M., WANG, C., MATANA AGUIAR, G. & BUCCI, M. 2022 The wall heat flux partitioning during the pool boiling of water on thin metallic foils. *Appl. Therm. Engng* **200**, 117638.

https://doi.org/10.1017/jfm.2026.11566 Published online by Cambridge University Press